Methane leak detection and sizing over long distances using dual frequency comb laser spectroscopy and a bootstrap inversion technique

Caroline B. Alden[1,2*], Subhomoy Ghosh[3], Sean Coburn[1], Colm Sweeney[2,4], Anna Karion[3], Robert Wright[1], Ian Coddington[3], Kuldeep Prasad[3], Gregory B. Rieker[1]

[1]Department of Mechanical Engineering, University of Colorado at Boulder, Boulder, CO, 80309 USA
[2]Cooperative Institute for Research in Environmental Sciences, Boulder, CO 80309, USA
[3]National Institute of Standards and Technology (NIST), Gaithersburg, MD, 20899, USA
[4]National Oceanic & Atmospheric Administration (NOAA), Boulder, CO 80305, USA

Correspondence to: Caroline B. Alden (caroline.alden@colorado.edu)

Abstract. Advances in natural gas extraction technology have led to increased activity in the production and transport sectors in the United States, and, as a consequence, an increased need for reliable monitoring of methane leaks to the atmosphere. We present a statistical methodology in combination with an observing system for the detection and attribution of fugitive emissions of methane from distributed potential source location landscapes such as natural gas production sites. We measure long (>500 m), integrated open path concentrations of atmospheric methane using a dual frequency comb spectrometer and combine measurements with an atmospheric transport model to infer leak locations and strengths using a novel statistical method, the non-zero minimum bootstrap (NZMB). The new statistical method allows us to determine whether the empirical distribution of possible source strengths for a given location excludes zero. Using this information, we identify leaking source locations (i.e., natural gas wells) through rejection of the null hypothesis that the source is not leaking. The method is tested with a series of synthetic data inversions with varying measurement density and varying levels of model-data mismatch. It is also tested with field observations of 1) a non-leaking source location and 2) a source location where a controlled emission of 2.1 E-5 kg s^{-1} of methane gas is released over a period of several hours. This series of synthetic data tests and outdoor field observations using a controlled methane release demonstrate the viability of the approach for the detection and sizing of very small (<2 g m^{-1}) leaks of methane across large distances (4+ km^2 in synthetic tests). The field tests demonstrate the ability to attribute small atmospheric enhancements of 18 ppb to the emitting source location against a background of combined atmospheric (e.g., background methane variability) and measurement uncertainty of 6 ppb (1-sigma), when measurements are averaged over 2 minutes. The results of the synthetic and field data testing show that the new observing system and statistical approach greatly decreases the incidence of false alarms (that is, wrongly identifying a well site to be leaking) compared with the same tests that don't use the NZMB approach, and therefore offers increased leak detection and sizing capabilities.

1 Introduction

The combustion of natural gas in high-efficiency power cycles is cleaner and produces less climate-warming carbon dioxide gas than the combustion of coal (Environmental Protection Agency, 2015), which has led to interest in natural gas as a cleaner alternative to coal for energy generation. Advances in natural gas extraction technology have led to a 35% increase in

5 total natural gas production between 2005 and 2013 in the United States (U.S. Energy Information Administration, 2015). Production is expected to increase by 45% above 2013 levels by the year 2040 (U.S. Energy Information Administration, 2015). A caveat to the promise of natural gas as a lower climate impact energy source, however, is that leaks of methane during extraction and delivery can result in climate warming. Methane gas has high global warming potential: much higher, for example, than carbon dioxide. Above a low threshold (~3.2%) leak rate from well to power plant, the near-term climate

10 impacts of using natural gas for power generation become worse than coal (Alvarez et al., 2012; Hayhoe et al., 2002). Recent system-wide analysis suggests that natural gas sector leak rates are likely higher than inventory estimates (Brandt et al., 2014; Zavala-Araiza et al., 2015a). To achieve the lower climate impacts and greater economic benefits of domestic natural gas production, it is important to find low cost methods to detect and reduce methane leakage (Alvarez et al., 2012).

15 The current industry practice for leak detection and repair (LDAR) is to perform infrequent (annual or less for most sites) "spot" checks for leaks, for example by visual inspection with an optical gas imaging (OGI) camera. However, recent work has shown that methane concentrations measured by OGI cameras can be drastically underestimated if conditions are not ideal, for example if temperatures are cold, wind speeds are high, or viewing distances are greater than 50 m (Ravikumar et al., 2016). Furthermore, spot check monitoring is inadequate for detection of leaks, given strong evidence for intermittency

20 of leaks (Allen et al., 2013, 2015; Mitchell et al., 2015; Subramanian et al., 2015). It has been observed that a small number of facilities leaking at very high rates – so-called "super-emitters" (Frankenberg et al., 2016; Rella et al., 2015; Zavala-Araiza et al., 2015b) – can account for a majority of total emissions (Allen et al., 2013, 2014, 2015; Brandt et al., 2014), further underscoring the importance of continuous monitoring for leaks over large areas. Field campaigns with sophisticated atmospheric sampling techniques provide valuable snapshots of the state of natural gas development facility leaks (e.g.

25 Brantley et al., 2014; Karion et al., 2013), but it would be too costly to employ such measurement strategies for long-term continuous monitoring of most natural gas sector facilities.

We present and test an atmospheric measurement and inversion approach for detecting and quantifying emissions of methane that is composed of a long-range open-path laser situated in the center of a field of well sites, and a series of retroreflectors

30 around the perimeter of the field to direct light back to a detector co-located with the laser. The concentration of trace gases along the open beam path is determined from the species-specific absorption of light (Dobler et al., 2015; Flesch et al., 2004; Groth et al., 2015; Hashmonay et al., 1999; Levine et al., 2016). The laser is a dual frequency comb spectrometer: a unique broadband, high-resolution spectrometer that offers very high stability (low drift) and measurement reproducibility (close

agreement of measurements under different conditions, with different instruments or in different locations) of the trace gas measurement, so that concentrations can be compared across different conditions and across long periods of time. Laboratory and initial field measurements made with the dual frequency comb spectrometer indicate extremely low measurement uncertainty (3 ppb or lower measurement repeatability) over long pathlengths (Coburn, n.d.; Rieker et al., 2014; Truong et

5 al., 2016; Waxman et al., 2017). The combination of low uncertainty and high stability enable new opportunities for detection and sizing of even very small emissions of methane. Furthermore, the demonstration of sensitive methane measurements over kilometer-scale open paths allows for monitoring methane concentrations over large areas such as natural gas production, processing, and distribution sites.

10 While frequency comb measurements have previously been made in laboratory settings, the recent work of (Coburn, n.d.) along with the new work shown here demonstrate the viability of dual frequency comb spectroscopy in real-world conditions.

We use dual frequency comb measurements in a series of synthetic data and field data tests to demonstrate the utility of the

15 observing system and a novel statistical method for accurately locating one or more point sources of methane within a large area (4+ km^2) using distributed measurements of methane concentrations and an atmospheric transport model. The source-attribution method used here is to apply a non-negative least-squares fitting technique to solve for methane flux at a series of potential source locations (e.g., well heads, pads or other components), given a set of atmospheric observations and knowledge of atmospheric transport (Leuning et al., 2008). The new statistical approach, called the non-zero minimum

20 bootstrap method (NZMB), uses a bootstrapping of model uncertainties in order to produce an empirical distribution of source strength for a given well site. Specifically, the empirical distribution is obtained by performing multiple atmospheric inversions (or least-squares fits) using a set of resampled atmospheric measurements. The NZMB method establishes a criterion by which well sites or facilities are identified as having non-zero methane emissions based on examination of the minimum value of an ensemble of inversions. That is, a potential leak site is positively identified as a source of methane to

25 the atmosphere if the empirical cumulative distribution of likely source strengths (determined with a series of bootstrap operations) does not include a minimum threshold flux such as zero. Similarly, a facility is identified as not leaking if the empirical cumulative distribution of likely source strengths does include the minimum threshold flux (that is, the minimum value of all bootstrap operations is, for example, zero). By defining a specific null value for each potential leak, this approach reduces the incidence of false positive leak identification (the incorrect attribution of a methane source to a non-

30 leaking facility or well), compared with the same tests that do not use the NZMB method (the "non-bootstrap" approach). For comparison, we run the same series of tests with the non-bootstrap approach, which approximates emissions using a single non-negative least-squares fit.

This work presents a set of synthetic experiments and a set of field tests with a controlled leak to prove the utility of this novel observing system for the detection and sizing of methane leaks.

Field tests with atmospheric observation data are performed in a 3 km x 2.5 km field site located in north-central Colorado
5   over the course of one day in January, 2017. Measurements are made along a series of 3 beams extending from a spectrometer in the middle of the domain. Synthetic data tests assess the effects of increasing measurement density (4, 8, 16, 32, and 64 beams), and the effects of increasing model data mismatch (that is, "observation" noise arising from measurement, transport and other uncertainties).

10   We define leak identification success as maximizing the incidences of leaks found, with a minimal occurrence of false positive source identification, enabling quick response to leaks and avoiding costly mobilization of repairs teams due to false positive leak identification. The ability to correctly ascertain the absence of a leak is therefore of equal importance to the ability to find leaks, for regulatory compliance applications of this method. With the above tests, we therefore seek to determine 1) whether methane point source emissions can be detected and sized under conditions of observational
15   uncertainty (model-data mismatch) and background variation, 2) whether the absence of a leak can be ascertained in an outdoor field setting, 3) whether the NZMB method allows for leaks to be positively identified under scenarios of greater simulated noise, compared with the non-bootstrap method, and 4) whether higher density of observations increases likelihood that the NZMB and non-bootstrap methods can positively identify leaks. The success of the synthetic and field data tests demonstrates the potential of this observing system for continuous monitoring applications, such as for natural gas
20   facilities, and for providing emission source locations and their approximate strengths. The experiments here also demonstrate the potential for this technology to be used for other source estimation and monitoring applications, for example carbon sequestration.

2 Methods

2.1 Gaussian plume atmospheric transport model

25   In both the synthetic and real data tests, atmospheric transport is simulated using a Gaussian plume model, using Pasquill-Gifford parameterization of plume dispersion in the lateral and vertical directions (Green et al., 1980; Griffiths, 1994; Hanna et al., 1982). Micrometeorology in the boundary layer is a non-trivial source of uncertainty for characterization of atmospheric flow, and the Gaussian Plume model represents a highly-simplified representation of atmospheric transport and dispersion. It has been used to characterize the mean state of source-receptor relationships with a point source as long as the
30   transport time from source to receptor is comparable to the data averaging time (Gifford, 1976; Hirst et al., 2004), and measurements that integrate concentrations across space, such as those presented here, make the simulation of atmospheric flow with a Gaussian plume model more suitable than for measurements that are discrete in space. We select the plume

model for assessment of the NZMB method, rather than implementing more advanced representations of transport, because of its simplicity and low computational cost. Future campaigns aimed at quantification of true emissions will benefit from an assessment of the drawbacks inherent in Gaussian plume model characterization of atmospheric transport, or use of a more sophisticated model, particularly for measurements made at short range.

For the synthetic data tests, the choice of transport model is largely trivial, given that transport is considered "perfect". Even so, the synthetic data tests assume a constant methane source to the atmosphere through time, and measurement frequency that is comparable to the travel time from source to measurement location. Field data is collected under similar conditions, such that measurement frequency, lateral distance from leak location to beams, and constancy of leak rate make the Gaussian

10 plume model an appropriate if simplified choice of transport model (Gifford, 1976; Hirst et al., 2004). Because the purposes of the study here are to confirm or reject the basic methodology and not to investigate the impacts of micrometeorological representation on the ability to estimate fluxes, we find the plume model to be sufficient.

Neglecting influence of background methane concentrations, Eq. (1) shows the relationship between fluxes and atmospheric

15 concentrations (e.g. Leuning et al., 2008):

$$\mathbf{c} = \mathbf{x} * (\mathbf{c}/\mathbf{x})_{modeled} , \tag{1}$$

Where the $n \times 1$ vector $\mathbf{c}$ is the atmospheric concentration of the constituent of interest at various points in space, and n is the

20 number of measurements. The vector $\mathbf{x}$ is $m \times 1$ surface sources of the constituent (flux units), where the size of m is equal to the number of potential source flux locations. The value $(\mathbf{c}/\mathbf{x})_{modeled}$ is an influence function describing the relationship between source emissions and concentrations at observation points (spectrometer beams) under different meteorological conditions, derived using the Gaussian plume model. The matrix $(\mathbf{c}/\mathbf{x})_{modeled}$ is the transport operator matrix representing source-receptor relationships, commonly written as $\mathbf{H}$ (that convention will be followed here).

25 **2.2 Dual Frequency Comb spectrometer for long-range open path methane detection**

Dual frequency comb spectrometer measurements are made by transmitting light from the spectrometer through open air at a discrete set of wavelengths where methane absorbs light. The light is transmitted in the direction of a retroreflector, which can be placed 1+ km away (Coburn et al., n.d.; Rieker et al., 2014; Truong et al.; Waxman et al.). The retroreflector directs light back toward a detector co-located with the spectrometer. The amount of light that is absorbed by methane yields a

30 direct measurement of the average mole fraction of methane along the open path from spectrometer to retroreflector. The measurements presented here are part of the first ever campaign to measure atmospheric concentrations with a dual frequency comb spectrometer in a field environment (Coburn, n.d.).
tempus lorem.

2.3 Flux estimation with Non-Negative Least-Squares fitting solution

We use the Non-Negative Least-Squares (NNLS) algorithm in Fortran-90 to solve for a flux rate, given atmospheric observations (synthetic or real) and atmospheric transport influence functions (Lawson and Hanson, 1995). This algorithm iteratively solves for the best-fit $m \times 1$ vector of fluxes, $\mathbf{x}$, given an $n \times 1$ vector of data measurements, $\mathbf{y}$, and an $n \times m$

5   matrix of influence functions, $\mathbf{H}$. Given $\mathbf{H}$ and $\mathbf{y}$, the NNLS algorithm attempts to solve the least squares problem for the vector $\mathbf{x}$ (i.e., methane emission rate at each well site):

$\mathbf{Hx} = \mathbf{y}$, subject to $\mathbf{x} >= 0$ (2)

Uncertainties in $\mathbf{x}$ and $\mathbf{y}$ are not included in the NNLS fit; model-data mismatch is used only in generation of the synthetic observations, and not as a control on the solution for $\mathbf{x}$. The NNLS algorithm not only returns the solution vector, $\mathbf{x}$, but also

10   $\mathbf{Hx}$, an $n \times 1$ vector describing the expected atmospheric concentration given $\mathbf{H}$ and the solution for $\mathbf{x}$.

2.4 Non-Zero Minimum Bootstrap Analysis

The non-zero minimum bootstrap analysis is a statistical test of the null hypothesis ($Hypothesis_0$) that the source strength at a given well site is equal to 0 kg s^{-1}. It is used here to estimate source strengths in both the synthetic and field data tests. For each of m potential source locations:

15                              $Hypothesis_0 : x_j = 0 \ \ (j = 1,\ldots,m)$

                              $Hypothesis_1 : x_j > 0 \ \ (j = 1,\ldots,m)$

Given that model-data mismatch uncertainty is not zero (i.e., there is uncertainty in the exact relationship between atmospheric observations and surface fluxes due to transport, measurement and other uncertainties), it is not expected that the NNLS fit of $\mathbf{Hx}$ to $\mathbf{y}$ is exact, although the problem is overdetermined. We therefore use the mismatch between $\mathbf{Hx}$ and $\mathbf{y}$

20   to create an empirical distribution function describing the confidence interval of the fit to the data, and to accept or reject the null hypothesis claim that we have enough evidence to claim that a particular source is not leaking. We rely on the assumption that model-data mismatch uncertainty has an un-biased Gaussian distribution. This bootstrapped analysis is described in more detail next.

25   The method for employing the bootstrap analysis is as follows. We first solve for surface-to-atmosphere fluxes of CH$_4$, $\mathbf{x}$, using NNLS, as described in Sect. 2.3. Second, for each observation, y_i ($i = 1,\ldots,n$), we calculate the residual values from the fit to the NNLS solution:

$\epsilon_{\mathbf{R}i} = y_i - \hat{y}_i$,   (3)

where $\hat{y}_i$ ($i = 1,\ldots,n$) are the individual values in the vector $\mathbf{Hx}$.

The next step in the NZMB method is: for each observation, y_i ($i = 1,\ldots,n$), we generate 1000 new estimates of y_i by sampling residuals of the fit to the atmospheric data (with replacement, meaning a given value can be sampled more than

once), and adding that randomly selected ϵ_R value to the observation, y_i, to create y_{bi} (Efron, 1979). This step results in 1000 vectors $\mathbf{y}_b$ (b denotes a bootstrapped value), or 1000 sets of observations $\{y_{bi}, ..., y_{bn}\}$, where $y_{bi} = y_i + \epsilon_{bi}$.

We use NNLS to solve for $\mathbf{x}$ for each of the 1000 resampled sets of observations, yielding 1000 individual solutions for $\mathbf{x}$.

5   The final step in the NZMB method is to apply the non-zero-minimum criterion to the 1000 bootstrap solutions for each member of $\mathbf{x}$. For each possible source location, the minimum value from the 1000-member bootstrap analysis is obtained. The non-zero-minimum criterion states that if the minimum bootstrap value for a given well location is 0 kg s^{-1}, then the source location is classified as having a leak rate of 0 kg s^{-1} (i.e., no leak). This criterion establishes, under null, whether or not 0 (< 0 is not possible since a non-negative least-squares fit is used) is included in the domain of the empirical cumulative

10   distribution function with non-zero mass, described by the 1000 solutions for each well site in $\mathbf{x}$. If zero is included in this distribution, then the null hypothesis ($\mathbf{x} = 0$) cannot be rejected. Conversely, if 0 is not included in the empirical cumulative distribution function for a given well site (x_j), then the null hypothesis can be rejected and it can be assumed that that well site is leaking. We use a large number of bootstrap members (1000) to ensure that the law of large numbers is met, and that the empirical cumulative distribution function is a close enough approximation of the true cumulative distribution function.

After having identified which source locations are non-zero sources to the atmosphere (i.e., leaking), the mean leak strength is estimated as the mean of the 1000 bootstrap solutions for that source location. Uncertainty in the strength of the true leak is calculated as the standard deviation of the 1000 bootstrap solutions at the true leak location.

20   This method requires little additional computational cost over the non-bootstrap NNLS approach, because additional runs of the transport model are not required, only additional inversions using resampling of the observations. The NZMB approach has the benefit of reducing false positive solutions while also gathering information regarding the parameters of the assumed Gaussian distribution.

2.5 Synthetic Data Tests and Results

25   #### 2.5.1 "True" leak locations and strengths

To prepare synthetic data testing of the NZMB method, we randomly distribute 20 possible leak source locations within a theoretical 2 km x 2 km domain. This is a reasonable approximation of well density based on high-production regions of the western United States (average well density across the Marcellus and Haynesville shale gas plays are 3+ wells km^{-2}). Of the 20 wells sites in the domain, we simulate a scenario in which 2 source locations are leaking. The "true" leak rate at well site

30   number 6 is 4.5E-5 kg s^{-1} and the "true" source at well site number 19 has a rate of 3.0E-5 kg s^{-1}. The remaining 18 well sites are assigned "true" leak strengths of 0 kg s^{-1} (Fig. 1). The two "true" leak strengths tested here are very small: roughly half

the size of the smallest leaks found by Rella et al. (2015) in a survey of oil and natural gas well pads. We assume that the height above ground level of each leak is 0 m.

2.5.2 Idealized meteorological conditions for synthetic data tests

The meteorological data used for synthetic data tests represents an idealized scenario in which many wind directions and a
5   variety of wind speeds occur during the sampling of each beam in the domain. Leak strengths are simulated to be constant through time, such that the time dimension of the meteorology does not need to be considered. This approach assumes that enough time has passed for all meteorological conditions to have occurred during the sampling of each beam, a condition that that eliminates complications in comparing synthetic cases with different beam orientations. The idealized meteorological field applies 216 unique wind conditions to all beams: three wind speeds (2 m/s, 3 m/s and 6 m/s) from 72
10   directions (from 5º to 360º, in 5º increments). The conditions represent a situation where, over a long period of time, many different wind conditions yield a variety of different measurements downwind of emissions.

2.5.3 Measurement system configuration and synthetic observations

The "synthetic" atmospheric measurements are simulated based on the dual frequency-comb spectrometer observing system composed of a series of retroreflectors, and a light detector collocated with the spectrometer as described in Sect. 2.2. The
15   spectrometer is located in the center of the domain, at x = 1000 m and y = 1000 m (Fig. 2).

A "beam" is defined as the path between the spectrometer-detector system and a retroreflector. Configurations of 4, 8, 16, 32, and 64 beams per spectrometer-detector system are tested. In all beam configurations, retroreflectors are placed at an equal distance (1000 m) from the spectrometer and at equal distances from neighboring retroreflectors (e.g., Fig. 2). The hub-and-spoke beam configuration is a simple and repeatable pattern for comparison of different numbers of beams. The
20   height of the spectrometer and retroreflectors is 3 m above ground level. Figure 2 shows beams, beam end point locations (retroreflectors) and the spectrometer in a case with 16 beams.

"True" atmospheric methane concentrations are simulated by combining knowledge of atmospheric transport with knowledge of "true" sources and measurement (beam segment) locations with Eq. (1).

In order to generate the synthetic measurement data, each beam path is discretized into 100 segments. For each unique wind condition, "true" source fluxes are multiplied by **H** to calculate atmospheric enhancements at each of the 100 points along the beam path. Enhancements due to leaks are calculated independently for each segment of a beam and subsequently averaged for each beam and for each wind condition. This value mimics the actual data output of the spectrometer, which
30   measures the average concentration along the beam length.

The influence functions describing the relationships between each element of **x** and each segment of each beam path for each wind condition, **H**, are created using the Gaussian plume model described in Sect. 2.1, with neutral stability conditions (Pasquill category D). We create a vector of "true" atmospheric values, **c**, using Eq. (1).

2.5.4 Perturbation of observations with model-data mismatch noise

5   Model-data mismatch is the difference between the true atmospheric CH_4 concentration, **c**, and the simulated or measureable atmospheric CH_4 concentration. This difference is expected to be non-zero due, for example, to measurement uncertainty (sampling and instrumental error), transport uncertainty (imperfect knowledge of air flow between source and observation points), and representation error (for example, the assumption that the measured segment of beam appropriately characterizes the atmospheric concentration at the time and space scales that it represents in the model). We assume here that uncertainty

10   due to imperfectly known background concentration is also part of model-data mismatch uncertainty. We simulate progressively larger levels of model-data mismatch in order to identify differences in model capabilities to locate and size leaks between the NZMB and non-bootstrap methods.

A range of model-data mismatch values are tested with the expectation that both the NZMB and non-bootstrap models will

15   be more likely to locate and source leaks when lower model-data mismatch is added to the data. To simulate different possible magnitudes of model-data mismatch, the simulated true atmospheric concentrations, **c**, are perturbed with random Gaussian noise with mean 0 ppb and standard deviation equal to the following values: 0.1, 0.2, 0.3, 0.4, 0.5, 1.0, 1.5, 2.0, 2.5, 3.0, 3.5, 4.0, 4.5, 5, 6, 7, 8, 9, and 10 ppb, over a 1 km path. Measurement noise alone is expected to be on the order of 3 ppb or lower for a 1 km path (Rieker et al., 2014), although recent technological developments may drive measurement

20   uncertainties lower (Coburn et al., in prep). As the results of field tests will show, the range of model-data mismatch values tested are an appropriate approximation of observed noise. Model-data mismatch noise is assumed to be uncorrelated, following convention and understanding of the dual frequency comb measurement scheme. In Eq. (4), **ε** is a vector of model-data mismatch uncertainty corresponding to the vector, **c**. Both vectors are of length n ($i =1,…,n$), where n is the number of observations. The vector **y** contains the synthetic observations, or the true atmospheric concentrations perturbed with

25   measurement noise.

$$\mathbf{y}_i = \mathbf{c}_i + \boldsymbol{\epsilon}_i \qquad\qquad (4)$$

2.6 Field Data Observations

2.6.1 Description of field deployed dual comb setup

The first measurements from a field deployed dual frequency comb spectrometer are from the NOAA/ESRL Table Mountain

30   Test Facility, 10 km north of Boulder, Colorado (Fig. 3) (Coburn, n.d.). The spectrometer is located near the center of a large (~3 x 2.5 km) flat-topped mesa that rises several meters above the surrounding terrain (see Fig. 3). The dual frequency comb

is housed inside of a trailer, with telescope pitch and catch apparatus affixed to a rotating gimbal on the trailer roof (roughly 4 meters above ground level). The actual dual frequency comb spectrometer is contained in a 56 x 56 x 61-cm electronics rack, and the large trailer provides a field deployment home base. The beam pitch and catch system sends light between 1620 and 1680 nm, with discrete line spacing of 0.002 nm, through a 2-inch telescope. The power of returned light that reaches the

5   detector is approximately 200 µW (~8% of launched light), resulting in a laser system that emits and senses approximately 28,900 individual comb teeth, or absorption lines probed (Coburn, n.d.; Rieker et al., 2014; Sinclair et al., 2015). The wavelength "window" to which the instrument at Table Mountain is tuned is ~ 50 nm, spanning 625 individual CH_4 features, 2,482 CO_2 features, and 133 H_2O features. Intensity feedback, triggered data acquisition, and onboard phase correction are quasi-autonomous, enabling the system to operate continuously for long periods of time (Coburn, n.d.; Truong et al., 2016;

10   Waxman et al., 2017).

2.6.2 Leak location and strength

For the field experiments at Table Mountain, a cylinder of compressed methane gas is placed along a dirt road (for access) roughly 528 m away from the spectrometer (Fig. 3) and 1 meter above ground level. The methane cylinder is outfitted with a regulator and an Alicat mass flow controller (MC-20SLPM-D). The flow controller is set to release methane in a controlled

15   flow of 2.1 E-5 kg s^{-1} at source location 1, between 10:08 and 16:30 on January 26, 2017. The flow rate at source location 2 was set to 0.0 kg s^{-1} through the duration of January 26, 2017. The controlled methane release point is roughly 0.43 cm in diameter and oriented horizontally pointed toward the northeast, such that the velocity of gas exiting the tubing is negligible.

Importantly, the field tests are arranged so as to approximate the synthetic tests as closely as possible. To emulate the

20   "perfect" background condition of the synthetic tests, the background methane concentration for each source location is measured directly by an upwind beam. Because the background is assumed to be unique for each source location, each inversion includes only that source location in its solution for fluxes. That is, one inversion is performed for source location 1, and a separate inversion is performed for fluxes at source location 2.

2.6.3 Retroreflector locations

25   Three corner-cube retroreflectors ("retros") are located near source locations 1 and 2 at Table Mountain (see Fig. 3). At their nearest points, the lateral distances between beams 1 and 2 and source location 1 are 11 m, and 6 m, respectively. The minimum lateral distances between leak location 2 and beams 2 and 3 are 12 m and 8 m, respectively. The horizontal distance from the spectrometer to each retroreflector is 584 m, 585 m, and 588 m, respectively for retros 1, 2 and 3. All retroreflectors are positioned 1 meter above ground level.

2.6.4 Meteorology at Table Mountain

Wind speed and wind direction are measured directly with a 3D Sonic Anemometer (RM Young 81000 Ultrasonic 3D Anemometer with manufacturer-specified accuracy of ± 0.05 m s^{-1}) located mid-way between the spectrometer and the retroreflectors. The suitability of the Gaussian plume model for short-range simulations decreases under low speeds, so all

5 data taken at wind speeds below 0.8 m s^{-1} was removed from this analysis.

2.6.5 Measurements

We test the bootstrap methodology using measurements taken over the course of one day in January 2017. We test the ability of the bootstrap approach to both disprove the null hypothesis (i.e., to correctly ascertain the presence of a non-zero methane emission) and to prove the null hypothesis (i.e., to correctly ascertain the absence of a leak), by gathering measurements

10 along beam paths that bound: 1) source location 1, where methane is released in a controlled flow rate of 2.1 E-5 kg s^{-1}, and 2) source location 2, where no methane is released. Quasi-continuous (626 Hz) data acquisition occurs for 2 minutes on each beam. Time-averaging over 2 minutes is performed to maximize gains in measurement precision as well as to average across shorter time scale eddy mixing events. After a measurement is taken, less than 30 seconds elapse while the gimbal moves to focus the beam on the next retroreflector in the measurement sequence. The measurement sequence for the time period of

15 study on January 26, 2017 is: retro 1, retro 2, retro 1, retro 3, retro 1, retro 2, and so on. A fourth retroreflector is included in the measurement sequence (leading to a small time delay between measurements made on retro 3 and retro 2), but data from that beam is not analyzed here for simplicity.

2.6.6 Background CH$_4$ Estimation

To most closely approximate the synthetic data testing framework in the field environment, we directly sample background

20 CH$_4$ concentrations upwind of the leak point. The array of beams shown in Fig. 3 "sandwich" each source location. This configuration means that under most wind conditions (wind directions within ~40º of orthogonal to the beam array in either direction), one beam is situated upwind and one beam is situated downwind of each source location. With this method, we can remove the time-varying CH$_4$ concentration to which enhancements from discrete near-field emissions are added. While the Table Mountain site is relatively removed from expected anthropogenic and biogenic methane sources, the presence of

25 nearby small livestock and oil and gas operations means that the background methane concentration does vary according to wind direction and through time. The "beam sandwich" approach, of placing beams on either side of each source location, represents a plausible solution to future regional-scale monitoring of many potential emitters.

3 Results of Synthetic Data Tests

3.1 Synthetic source location with and without the NZMB method

We calculate solutions for **x** using NNLS in a single solution without a bootstrap approach for each set of beam configurations and for each model-data mismatch scenario in the synthetic data case. Figure 4 summarizes the findings of each test by categorizing the results into four outcomes: 2 true leaks found with no false positives, 1 true leak found with no false positives, 0 true leaks found with no false positives, and 1 or more true leaks found with 1 or more false positive. The top half of Fig. 4 (for the non-bootstrap method) shows that, of the 5 different beam configurations tested, all result in false positive source locations under every model-data mismatch scenario when a non-bootstrap approach is taken. That is, even with very low model-data mismatch (0.1 ppb) and many beam measurement locations (64), the non-bootstrap method fails to positively identify true leak sources without also generating false positive results. Non-zero solutions are found for source locations where no "true" leak exists.

The bottom half of Fig. 4 shows the results of the same tests, using instead the NZMB method for locating leaks. The results show that success in leak detection is much higher using NZMB, compared with the non-bootstrap tests. Indeed, none of the NZMB tests result in the occurrence of a false-positive leak location, and only tests with low numbers of beams relative to the number of source locations (4 and 8 beam cases) fail to find both of the true leaks. The 4-beam case results in positive identification of both leaks up to a model-data mismatch threshold of 2 ppb, above which 1 true leak is found. One leak is consistently found up to a threshold of 5 ppb, and above 5 ppb model data mismatch no true leaks are identified (but no false positives are generated either). The 8-beam case results in accurate location of both true leaks up to a model-data mismatch threshold of 3.5 ppb, above which 1 true leak is found (with no false positives). One leak is consistently found up to the maximum testing point of 10 ppb. In order to consistently locate both true leaks with no false positive results under all model-data mismatch scenarios, 16 or more beams are needed. Alternate configurations of "true" leaks at well sites other than 6 and 9 are not tested, however given that meteorological conditions are simulated equally from all directions, we would not expect a different set of results from a different set of "true" leaks.

The results for the 8-beam NNLS without bootstrap and the NNLS with NZMB cases are shown in Figs. 5 and 6. It is evident from Fig. 5 that, even with very low model-data mismatch noise (0.1 ppb), the non-bootstrap model results in well sites other than the 2 true leak locations being erroneously identified as sources of methane. By contrast, no false-positive leaks are identified in the NZMB case shown in Fig. 6. Above a model-data mismatch threshold of 4 ppb, only one of two true leaks are found in the 8-beam case using NSMB. As Fig. 4 shows, 16 or more beams are necessary to consistently find both true leaks at higher thresholds of model-data mismatch uncertainty using the NZMB method, given the hub-and-spoke beam placement scheme tested here. More complex placement of beams (for example placing beams closer to known well sites) would likely result in even better ability to locate leaks with fewer beams.

3.2 Synthetic source sizing using the NZMB method

Synthetic data tests of the new bootstrap methodology presented here show high success in leak location, with zero incidence of false positive leak detections. Following successful identification of leak locations with the NZMB method, leak sizes can be estimated using the statistical distribution of bootstrap operations. Figure 6 shows the maximum and minimum values of

5   1000 bootstrap operations for each model-data mismatch test case for the 8-beam configuration. At low levels of model-data mismatch uncertainty (e.g. 0.1-0.5 ppb), the maximum and minimum solutions bound a small range that is close to the true leak strength. As higher levels of model-data mismatch noise are added to observations, the maximum and minimum values diverge. However, even as the maximum and minimum solutions diverge, most cases include the true leak strength within the maximum and minimum bounds. As described in Sect. 2, we use the mean and standard deviation of 1000 operations to

10   estimate leak flow rate and uncertainty.

Using the NZMB method, all beam cases (even the 4-beam case) correctly identify that both well sites 6 and 19 are emitting methane when model-data mismatch is 2 ppb or lower (Fig. 4). At that level of model-data mismatch, higher numbers of beams and observations tend to lead to lower standard deviation around the mean estimated leak strength and a more

15   accurate estimate of true leak strength (Table 1). An exception is at well site 19, where the 8-beam case did not perform as well as the 4-beam case. It may be that both cases were inadequate for accurately sizing leaks, and that 16 beams are necessary in a dense field of wells such as is tested here. The failure of the 8-beam case to accurately predict the leak rate at well site 19 is also evident from histograms of bootstrap operations, shown for each beam case with model-data mismatch of 2 ppb in Fig. 7.

Histograms of the results for the 16, 32 and 64 beam cases with 10 ppb model-data mismatch are shown in Fig. 8. It is clear from Fig. 8 that, even with very high model-data mismatch uncertainty, simple hub-and-spoke configurations of between 16-64 beams are able to locate and estimate leak flow rates to within reasonable bounds of uncertainty.

4 Results of Field Data Tests

25   ### 4.1 Performance overview of field deployed DCS

Atmospheric observations are made over the course of one day in January, 2017 at the Table Mountain site. A set of 3 retroreflectors create long-range open-path beams of ~580 m (Fig 3). Spectrometer performance in the field demonstrates no loss of precision or reliability compared with laboratory performance, as demonstrated by (Coburn, n.d.). Figure 9 shows a plot of Allan deviations for January 26, 2017, demonstrating measurement precision of approximately 5 ppb when

30   measurements are averaged for 2 minutes. Precision is limited by repeatability of measurements and atmospheric variability of CH_4; the latter is likely a dominant driver of uncertainty in this case, as will be discussed in Sect. 5.2. The Allan deviation

in Fig. 9 shows improvement of precision with averaging time, to a minimum at ~70 seconds, followed by an increase that is likely due to atmospheric variability. We use 120 second averaged samples in this work, which corresponds to just under 6 ppb.

4.2 Atmospheric Observations of CH₄ at Table Mountain

5   On January 26, measurements are made throughout the day, including during a 6.5 hour-long controlled release of methane at one of two local source locations (1). At an adjacent source location (2), no methane release is emitted. A series of 3 retroreflectors are oriented such that each source region is monitored independently from the other; one beam on either side of each source location serves as a "background" measurement. We examine the results of two separate inversion tests: 1) a day-long set of observations of the source location with the controlled release that is situated between retroreflectors 1 and 2,

10   and 2) a day-long set of observations of a non-leaking source location situated between retroreflectors 2 and 3. These tests were performed simultaneously, such that contamination from source location 1 could have resulted in background contamination for monitoring of source location 2.

On January 26, 2017, mean wind speeds are 2.1 m/s and winds are primarily from the east and northeast, so that

15   retroreflector 1 is downwind of the controlled release, and retroreflector 2 is upwind of the controlled release. Similarly, retroreflector 2 is downwind of the non-leaking source location and retroreflector 3 is upwind of the non-leaking source (Fig. 3).

At source location 1 (Fig. 10, panel a), during the period when the controlled release is on (non-zero flow), the downwind

20   retroreflector (Retro 1) shows a clear enhancement above the concentration measured on the upwind retroreflector (Retro 2), except during the middle of the day when the winds shift briefly to the south (Fig. 10, panel c). The mean of all CH₄ measurements along beam 1 during the period that the leak is on is 2043 ppb; the mean CH₄ measured along beam 2 during the same period is 2026 ppb. Both retroreflectors demonstrate changes in background CH₄ concentrations over the course of the day; the range in values measured on the upwind retroreflector is 82 ppb. There appears to be some relationship between

25   ambient CH₄ concentration and wind direction, as both retroreflectors show a drastic decrease in concentration when the winds abruptly shift to the West at 16:30 (which happens to coincide with the time the leak was turned off).

At source location 2, no leak is released during the period of study, and throughout the course of the day, both retroreflectors 2 and 3 measure similar changes in atmospheric CH₄ variability (Fig. 10 panel b). The range of measured values over the

30   course of the entire day are 128 ppb on beam 2 and 126 ppb on beam 3. The mean of all CH₄ measurements (throughout the course of the day) is 2015 ppb on beam 2, and 2020 ppb on beam 3.

4.3 Background CH$_4$ Observations

The beams stationed upwind of each source location provide estimates of the background CH$_4$ concentration inflow for that site. At source location 1, the winds are such on January 26th that retro 2 is upwind, providing background concentration measurements for that location. At source location 2, retro 3 is the upwind or background concentration beam. We apply a

5 tolerance criteria of 5 minutes, so that for a measurement on beam 2 (3) to be used as the background for beam 1 (2), no more than 5 minutes can have elapsed between the middle points of the two measurement times. After each set of upwind and downwind measurements has been paired within this time window, the concentration measured on the upwind beam is subtracted from that measured on the downwind beam, to yield a measure of the CH$_4$ enhancement due to fluxes at the source location. Applying this method, the mean enhancement above background on retro 1 – which is downwind of source

10 location 1 (leak rate of 2.1E-5 kg s^{-1}) – is 18.0 ppb. Applying this method to source location 2, we find a mean enhancement on retro 2 – which is downwind of source location 2 (leak rate of 0 kg s^{-1}) – of 0.5 ppb, a value well within the range of variability expected from measurement uncertainty and background variability.

4.4 Field-based estimates of model-data mismatch

We examine measurements at source location 2 in order to estimate model-data mismatch in the field, for comparison with

15 the model-data mismatch values applied in the synthetic data tests. By examining the difference between measurements made on different retroreflectors (retros 2 and 3) at similar points in time (within 5 minutes), we obtain an approximation of the model-data mismatch arising from measurement representation uncertainties and background variability on the timescale relevant for estimation using this technique. We find a standard deviation of 6 ppb, which suggests that the range of model-data mismatch values tested in the synthetic data experiments are appropriate. The Allan deviation in Fig. 9 shows a similar

20 level of measurement uncertainty, which suggests that most of the uncertainty observed in our record is captured in this estimate of model-data mismatch, which includes effects of atmospheric variability. Precision could be improved by averaging data over a shorter time span (70 seconds), but those gains would be minimal (Fig. 9).

4.5 Results of inversions using Table Mountain observations

Both the Non-bootstrap and the NZMB approaches accurately predict the presence of methane emissions at source location 1

25 (Table 2). The average bootstrapped flux value is within 1-sigma of the true flux value measured at the flow meter at source location 1 (Fig. 11). At source location 2, the non-bootstrap approach falsely predicts a positive emission rate of 0.2 E-5 kg s^{-1} (Table 2) where no leak is present. The NZMB approach, by contrast, is able to accurately predict that there is no leak present at source location 2, because the minimum of the 1000 bootstrap solutions is zero (Fig. 11). As the synthetic data tests demonstrated, the NZMB method is necessary to avoid false identification of leaking source locations. The field data

30 tests corroborate that the new bootstrap approach enables higher confidence of accurate attribution of emissions to source locations without generating "false alarms".

5 Discussion

The results of this study demonstrate success of the new observing system in finding one or more leaks of methane in a field of wells, using synthetic and field data for confirmation. The methods presented here for locating and sizing leaks of methane in a field of natural gas production facilities succeeds not only in identifying the location of a leak, but it also does
5   so with no incidences of "false positive" leak detection in either the synthetic or field data tests.

5.1 Synthetic Data Tests

The results of the synthetic data tests demonstrate how the observing system tested in the field for a single source location can be expanded for simultaneous monitoring of many source locations. We find that synthetic tests performed without the NZMB methodology failed to identify the presence of leaks as reliably as synthetic tests performed with the NZMB method,
10   demonstrating that our new statistical methods are more robust for leak detection. In the non-bootstrap tests, all synthetic data cases resulted in false positive solutions (Fig. 4). By contrast, the NZMB method succeeds in correctly identifying two leaks of strength 3.0E-5 and 4.5E-5 kg s^{-1} with 4 or more beams monitoring 20 wells in a 4 km^2 area, with 2 ppb model-data mismatch uncertainty (a condition that could conceivably also be met in the field given low background uncertainty and high measurement precision). The NZMB method also consistently succeeds in finding both leaks with 16 or more beams with at
15   least 10 ppb model-data mismatch uncertainty. Notably, the NZMB method locates and sizes both leaks with no false positive results. Determination of leak strength was successful to within 25% (and all but a few cases well below 10%) for all cases with 16 or more beams, using the NZMB method.

5.2 Field Data Tests

Field data testing of the NZMB method corroborates the synthetic data findings: that the new atmospheric observing system
20   presented here results in high accuracy of leak detection without false positive results. The ability of the dual frequency comb spectrometer to identify a very small leak (2.1 E-5 kg s^{-1}), relying on very small methane enhancements (18 ppb) against a highly variable background (range of 82 ppb), demonstrates the potential power of this method for the methane leak detection over large areas.

6 Conclusions

25   The focus of this study is to show the powerful potential of dual frequency comb spectroscopy for the location and sizing of point source emissions. The synthetic and field tests presented here rely on near-perfect (in the synthetic data tests) or well-constrained (in the field data tests) background concentration estimation. Future studies are needed to address the potential complications of more complex background conditions and meteorological conditions under which it is not possible to obtain sequential "upwind" and "downwind" samples. Similarly, the tests here rely on the assumption of constant leak rates,
30   which is likely not a realistic assumption that can be made for methane emissions from oil and gas operations. Future work

to address these complexities will be necessary. Future studies are also needed to examine the gains that can be made from optimization of beam configurations for improved leak detection given variable wind and background conditions. Work aimed at addressing these complications is underway, as are inversion efforts to resolve issues of leak intermittency. The initial work presented here demonstrates the promising potential of dual frequency comb spectroscopy for detection of leaks

5   in the natural gas supply chain, and the valuable gains that can be provided by using the NZMB method over the NNLS fitting technique alone.

The authors declare that they have no conflict of interest.

Author Contribution

10   S. Ghosh, K. Prasad, and C. Alden developed the statistical NZMB technique. C. Alden, S. Coburn, R. Wright, C. Sweeney, K. Prasad, S. Ghosh and G. Rieker designed the experiments and S. Coburn, R. Wright, and C. Alden carried them out. A. Karion, S. Coburn and R. Wright provided expert guidance and experimental design input. C. Alden prepared the manuscript with contributions from all co-authors.

Data Availability

15   All data will be made publically available on an FTP server upon publication. This section will be updated with an address to that site.

Acknowledgements

The information, data, or work presented herein was funded in part by the Advanced Research Projects Agency-Energy (ARPA-E), U.S. Department of Energy, under Award Number DE-AR0000539. The views and opinions of authors

20   expressed herein do not necessarily state or reflect those of the United States Government or any agency thereof.

References

Allen, D. T., Torres, V. M., Thomas, J., Sullivan, D. W., Harrison, M., Hendler, A., Herndon, S. C., Kolb, C. E., Fraser, M. P., Hill, A. D., Lamb, B. K., Miskimins, J., Sawyer, R. F. and Seinfeld, J. H.: Measurements of methane emissions at natural gas production sites in the United States, Proc. Natl. Acad. Sci., 110, 17768–17773, doi:10.1073/pnas.1304880110, 2013.

25   Allen, D. T., Pacsi, A. P., Sullivan, D. W., Zavala-Araiza, D., Harrison, M., Keen, K., Fraser, M. P., Hill, A. D., Sawyer, R. F. and Seinfeld, J. H.: Methane emissions from process equipment at natural gas production sites in the United States: pneumatic controllers, Environ. Sci. Technol., 49(1), 630–640, doi:10.1021/es5040156, 2014.

Allen, D. T., Sullivan, D. W., Zavala-Araiza, D., Pacsi, A. P., Harrison, M., Keen, K., Fraser, M. P., Hill, A. D., Lamb, B. K., Sawyer, R. F. and Seinfeld, J. H.: Methane Emissions from Process Equipment at Natural Gas Production Sites in the United States: Liquid Unloadings, Environ. Sci. Technol., 49, 641–648, doi:dx.doi.org/10.1021/es504016r, 2015.

Alvarez, R. A., Pacala, S. W., Winebrake, J. J., Chameides, W. L. and Hamburg, S. P.: Greater focus needed on methane

5 leakage from natural gas infrastructure, Proc. Natl. Acad. Sci., 109(17), 6435–6440, doi:10.1073/pnas.1202407109, 2012.

Brandt, A. R., Heath, G. A., Kort, E. A., O'Sullivan, F., Petron, G., Jordaan, S. M., Tans, P., Wilcox, J., Gopstein, A. M., Arent, D., Wofsy, S., Brown, N. J., Bradley, R., Stucky, G. D., Eardley, D. and Harriss, R.: Methane Leaks from North American Natural Gas Systems, Science (80-.)., 343, 733–735, doi:10.1126/science.1247045, 2014.

Brantley, H. L., Thoma, E. D., Squier, W. C., Guven, B. B. and Lyon, D.: Assessment of Methane Emissions from Oil and

10 Gas Production Pads using Mobile Measurements, Environ. Sci. Technol., 48, 14508–14515, doi:dx.doi.org/10.1021/es503070q, 2014.

Coburn, S., Alden, C. B., Wright, R., Cossel, K., Baumann, E., Truong, G.-W., Giorgetta, F., Sweeney, C., Newbury, N. R., Prasad, K., Coddington, I. and Rieker, G. B.: Continuous regional trace gas source attribution, Nat. Commun., n.d.

Dobler, J., Zaccheo, T. S., Blume, N., Braun, M., Botos, C. and Pernini, T. G.: Spatial mapping of greenhouse gases using

15 laser absorption spectrometers at local scales of interest, Proc. SPIE, 9645, 96450K1-9645K13, doi:10.1117/12.2197713, 2015.

Efron, B.: Bootstrap methods: Another look at the jackknife, Ann. Stat., 7(1), 1–26, doi:10.1214/aos/1176344552, 1979.

Environmental Protection Agency: Inventory of U.S. greenhouse gas emissions and sinks: 1990-2013, Fed. Regist., 80(36), 9718, doi:EPA 430-R-13-001, 2015.

20 Flesch, T. K., Wilson, J. D., Harper, L. A., Crenna, B. P. and Sharpe, R. R.: Deducing Ground-to-Air Emissions from Observed Trace Gas Concentrations: A field trial, J. Appl. Meteorol., 43, 487–502, doi:10.1175/1520-0450(2004)043<0487:DGEFOT>2.0.CO;2, 2004.

Frankenberg, C., Thorpe, A. K., Thompson, D. R., Hulley, G., Kort, E. A., Vance, N., Borchardt, J., Krings, T., Gerilowski, K., Sweeney, C., Conley, S., Bue, B. D., Aubrey, A. D., Hook, S. and Green, R. O.: Airborne methane remote measurements

25 reveal heavy-tail flux distribution in Four Corners region, Proc. Natl. Acad. Sci., 113(35), 9734–9739, doi:10.1073/pnas.1605617113, 2016.

Gifford, F. A.: Atmospheric dispersion models for environmental pollution, in Lectures on Air Pollution and Environmental Impact Analysis, edited by D. A. Haigen, pp. 35–58, Boston, Mass., 1976.

Green, A. E. S., Singhal, R. P. and Venkateswar, R.: Analytic Extensions of the Gaussian Plume Model, J. Air Pollut.

30 Control Assoc., 30(7), 773–776, doi:10.1080/00022470.1980.10465108, 1980.

Griffiths, R. F.: Errors in the use of the Briggs parameterization for atmospheric dispersion coefficients, Atmos. Environ., 28(17), 2861–2865, doi:doi:10.1016/1352-2310(94)90086-8, 1994.

Groth, A., Maurer, C., Reiser, M. and Kranert, M.: Determination of methane emission rates on a biogas plant using data from laser absorption spectrometry, Bioresour. Technol., 178, 359–361, doi:10.1016/j.biortech.2014.09.112, 2015.

Hanna, S. R., Briggs, G. A. and Hosker, Rayford P, J.: Handbook on atmospheric diffusion., 1982.

Hashmonay, R. a., Yost, M. G., Mamane, Y. and Benayahu, Y.: Emission rate apportionment from fugitive sources using open-path FTIR and mathematical inversion, Atmos. Environ., 33(5), 735–743, doi:10.1016/S1352-2310(98)00228-3, 1999.

Hayhoe, K., Kheshgi, H. S., Jain, A. K. and Wuebbles, D. J.: Substitution of natural gas for coal: Climatic effects of utility
5   sector emissions, Clim. Change, 54, 107–139, doi:doi:10.1023/A:1015737505552, 2002.

Hirst, B., Gibson, G., Gillespie, S., Archibald, I., Podlaha, O., Skeldon, K. D., Courtial, J., Monk, S. and Padgett, M.: Oil and gas prospecting by ultra-sensitive optical gas detection with inverse gas dispersion modelling, Geophys. Res. Lett., 31, 1–4, doi:10.1029/2004GL019678, 2004.

Karion, A., Sweeney, C., Pétron, G., Frost, G., Michael Hardesty, R., Kofler, J., Miller, B. R., Newberger, T., Wolter, S.,
10 Banta, R., Brewer, A., Dlugokencky, E., Lang, P., Montzka, S. a., Schnell, R., Tans, P., Trainer, M., Zamora, R. and Conley, S.: Methane emissions estimate from airborne measurements over a western United States natural gas field, Geophys. Res. Lett., 40(16), 4393–4397, doi:10.1002/grl.50811, 2013.

Lawson, C. L. and Hanson, R. J.: Solving Least Squares Problems, Prentice-Hall, Jet Propulsion Laboratory., 1995.

Leuning, R., Etheridge, D., Luhar, A. and Dunse, B.: Atmospheric monitoring and verification technologies for CO2
15 geosequestration, Int. J. Greenh. Gas Control, 2(3), 401–414, doi:10.1016/j.ijggc.2008.01.002, 2008.

Levine, Z. H., Pintar, A. L., Dobler, J. T., Blume, N., Braun, M., Zaccheo, T. S. and Pernini, T. G.: The detection of carbon dioxide leaks using quasi-tomographic laser absorption spectroscopy measurements in variable wind, Atmos. Meas. Tech., 9(4), 1627–1636, doi:10.5194/amt-9-1627-2016, 2016.

Mitchell, A. L., Tkacik, D. S., Roscioli, J. R., Herndon, S. C., Yacovitch, T. I., Martinez, D. M., Vaughn, T. L., Williams, L.,
20 Sullivan, M., Floerchinger, C., Omara, M., Subramanian, R., Zimmerle, D., Marchese, A. J. and Robinson, A. L.: Measurements of Methane Emissions from Natural Gas Gathering Facilities and Processing Plants: Measurement Results, Environ. Sci. Technol., 49(20), 12602, doi:10.1021/acs.est.5b04018, 2015.

Ravikumar, A. P., Wang, J. and Brandt, A. R.: Are Optical Gas Imaging Technologies Effective For Methane Leak Detection?, Environ. Sci. Technol., acs.est.6b03906, doi:10.1021/acs.est.6b03906, 2016.

25 Rella, C. W., Tsai, T. R., Botkin, C. G., Crosson, E. R. and Steele, D.: Measuring emissions from oil and natural gas well pads using the mobile flux plane technique, Environ. Sci. Technol., 49(7), 4742–4748, doi:10.1021/acs.est.5b00099, 2015.

Rieker, G. B., Giorgetta, F. R., Swann, W. C., Kofler, J., Zolot, A. M., Sinclair, L. C., Baumann, E., Cromer, C., Petron, G., Sweeney, C., Tans, P. P., Coddington, I. and Newbury, N. R.: Frequency-comb-based remote sensing of greenhouse gases over kilometer air paths, Optica, 1(5), 290–298, doi:10.1364/OPTICA.1.000290, 2014.

30 Sinclair, L. C., Deschênes, J. D., Sonderhouse, L., Swann, W. C., Khader, I. H., Baumann, E., Newbury, N. R. and Coddington, I.: Invited Article: A compact optically coherent fiber frequency comb, Rev. Sci. Instrum., 86(8), doi:10.1063/1.4928163, 2015.

Subramanian, R., Williams, L. L., Vaughn, T. L., Zimmerle, D., Roscioli, J. R., Herndon, S. C., Yacovitch, T. I., Floerchinger, C., Tkacik, D. S., Mitchell, A. L., Sullivan, M. R., Dallmann, T. R. and Robinson, A. L.: Methane emissions

from natural gas compressor stations in the transmission and storage sector: Measurements and comparisons with the EPA greenhouse gas reporting program protocol, Environ. Sci. Technol., 49(5), 3252–3261, doi:10.1021/es5060258, 2015.

Truong, G.-W., Waxman, E. M., Cossel, K. E. C. C., Baumann, E., Klose, A., Giorgetta, F. R., Swann, W. C., Newbury, N. R. and Coddington, I. C.: Accurate frequency referencing for fieldable dual-comb spectroscopy, Opt. Express, 24(26),

5   30495–30504, doi:10.1364/OE.24.030495, 2016.

U.S. Energy Information Administration: Annual Energy Outlook 2015. [online] Available from: www.eia.gov/forecasts/aeo, 2015.

Waxman, E. M., Cossel, K. C., Truong, G.-W., Giorgetta, F. R., Swann, W. C., Coburn, S., Wright, R. J., Rieker, G. B., Coddington, I. and Newbury, N. R.: Intercomparison of Open-Path Trace Gas Measurements with Two Dual Frequency

10   Comb Spectrometers, Atmos. Meas. Tech. Discuss., 1(March), 1–26, doi:10.5194/amt-2017-62, 2017.

Zavala-Araiza, D., Lyon, D. R., Alvarez, R. A., Davis, K. J., Harriss, R., Herndon, S. C., Karion, A., Kort, E. A., Lamb, B. K., Lan, X., Marchese, A. J., Pacala, S. W., Robinson, A. L., Shepson, P. B., Sweeney, C., Talbot, R., Townsend-Small, A., Yacovitch, T. I., Zimmerle, D. J. and Hamburg, S. P.: Reconciling divergent estimates of oil and gas methane emissions, Proc. Natl. Acad. Sci., 112(51), 15597–15602, doi:10.1073/pnas.1522126112, 2015a.

15   Zavala-Araiza, D., Lyon, D., Alvarez, R. A., Palacios, V., Harriss, R., Lan, X., Talbot, R. and Hamburg, S. P.: Toward a Functional Definition of Methane Super-Emitters: Application to Natural Gas Production Sites, Environ. Sci. Technol., 49, 8167–8174, doi:10.1021/acs.est.5b00133, 2015b.
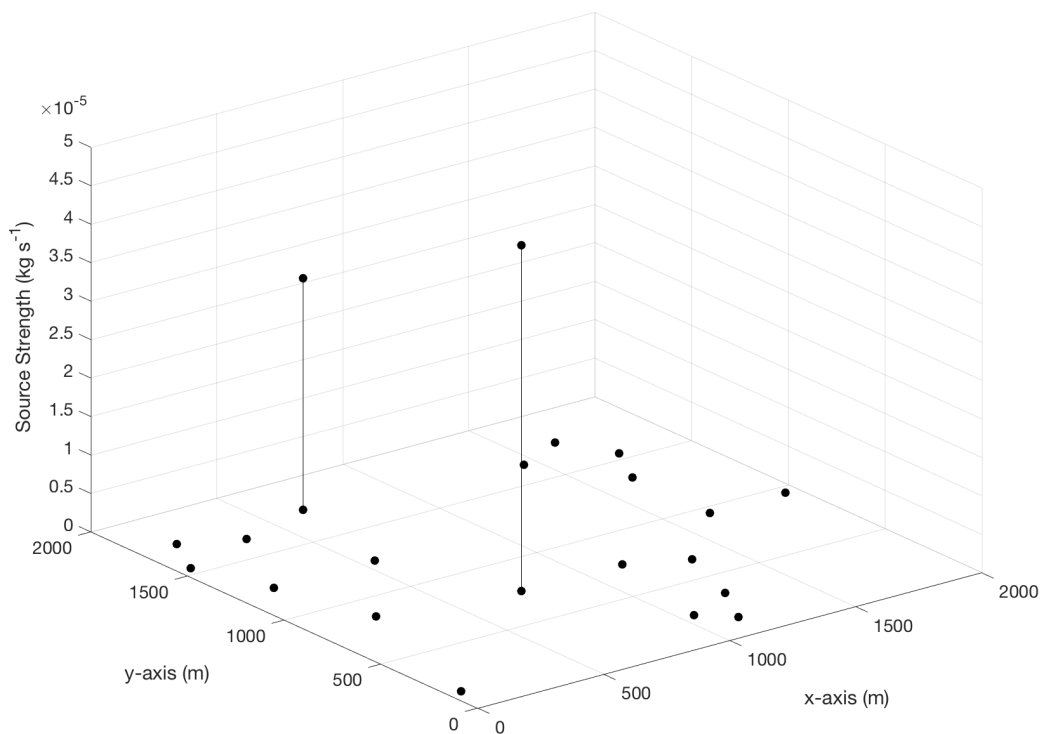
Figure 1: Synthetic test observation area: 2 km x 2 km domain with 20 source locations (black dots) at randomly distributed x and y locations (position shown on x and y axes). Of 20 point sources, well site 6 (x=750, y=750) and well site 19 (x=650, y=1750) have non-zero source strengths (shown on the z-axis).
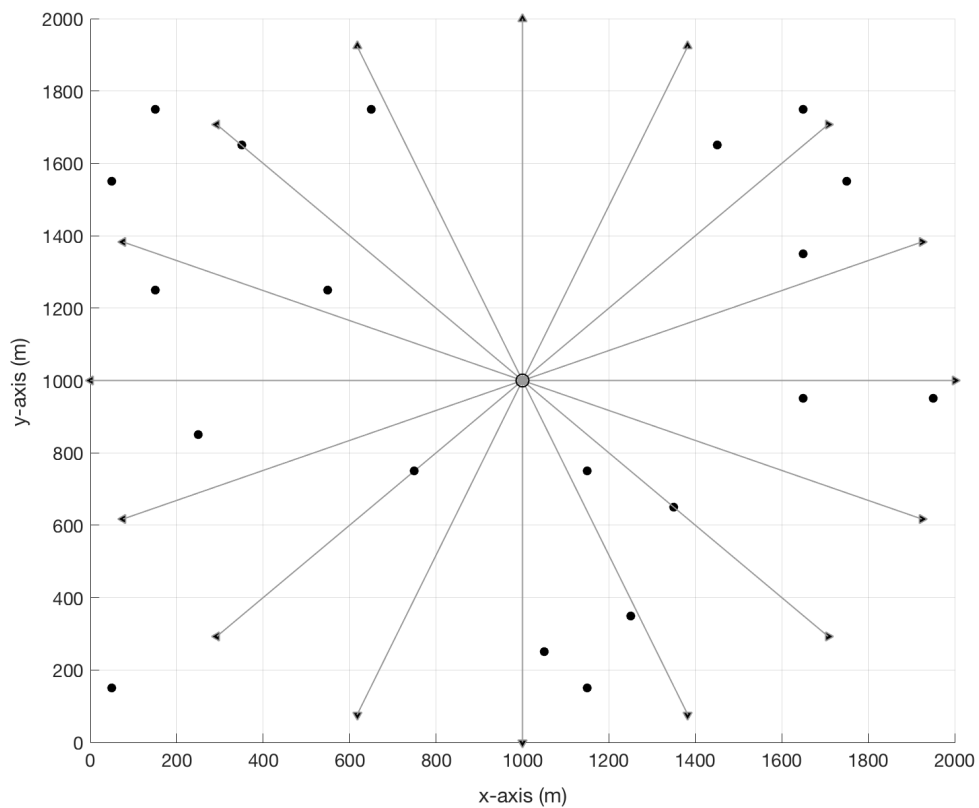
Figure 2: Map view of synthetic tests, with 20 source locations shown as black dots and 16 beams shown as gray lines that extend from the spectrometer (circle at x = 1000 m and y = 1000 m) to retroreflectors (black triangles).
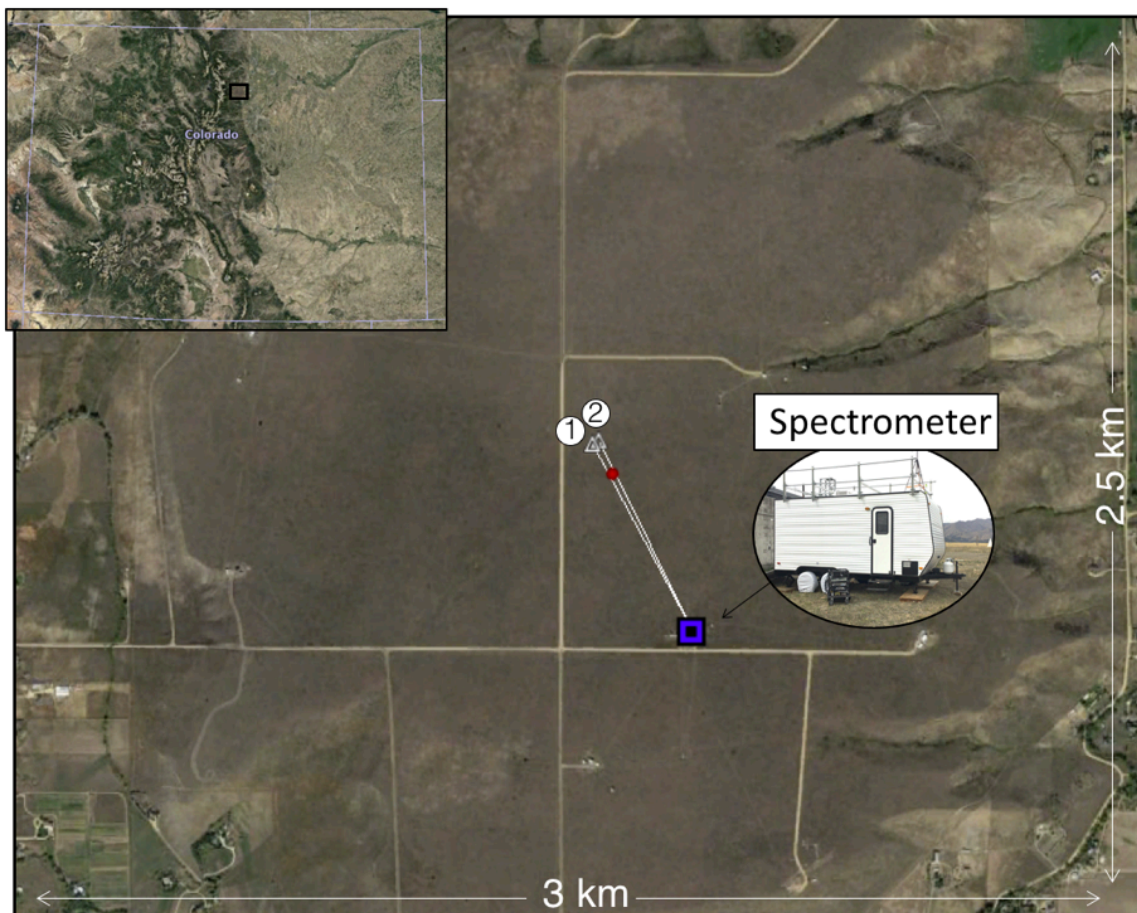
Figure 3: Map view of observation test site at Table Mountain, Colorado (upper left inset shows geographic location of test site), with two source locations (location 1, in red, between beams 1 and 2; location 2, in green, between beams 2 and 3) and three beams shown as white lines that extend from the spectrometer (blue square) to retroreflectors (white triangles, and labeled 1-3).
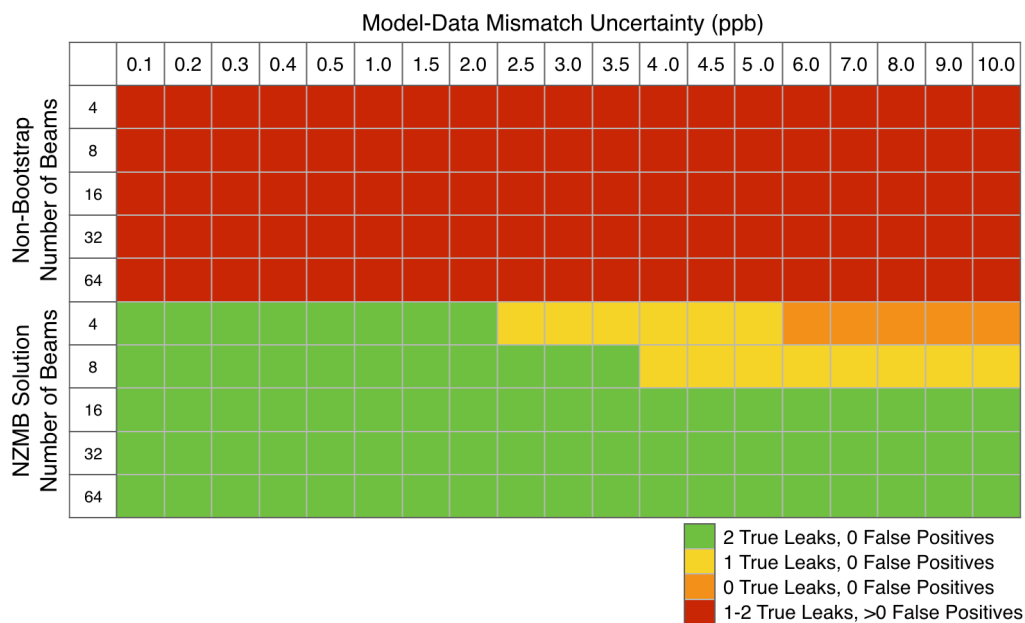
Figure 4: Summary of synthetic data test results. Top 5 rows show results of non-bootstrap inversions and bottom 5 rows show results of NZMB inversions for the 4, 8, 16, 32, and 64 beam cases. Columns indicate results for different values of model-data mismatch added as noise to the synthetic measurements. Color coding of cells indicates summary of model success, as detailed by the legend.
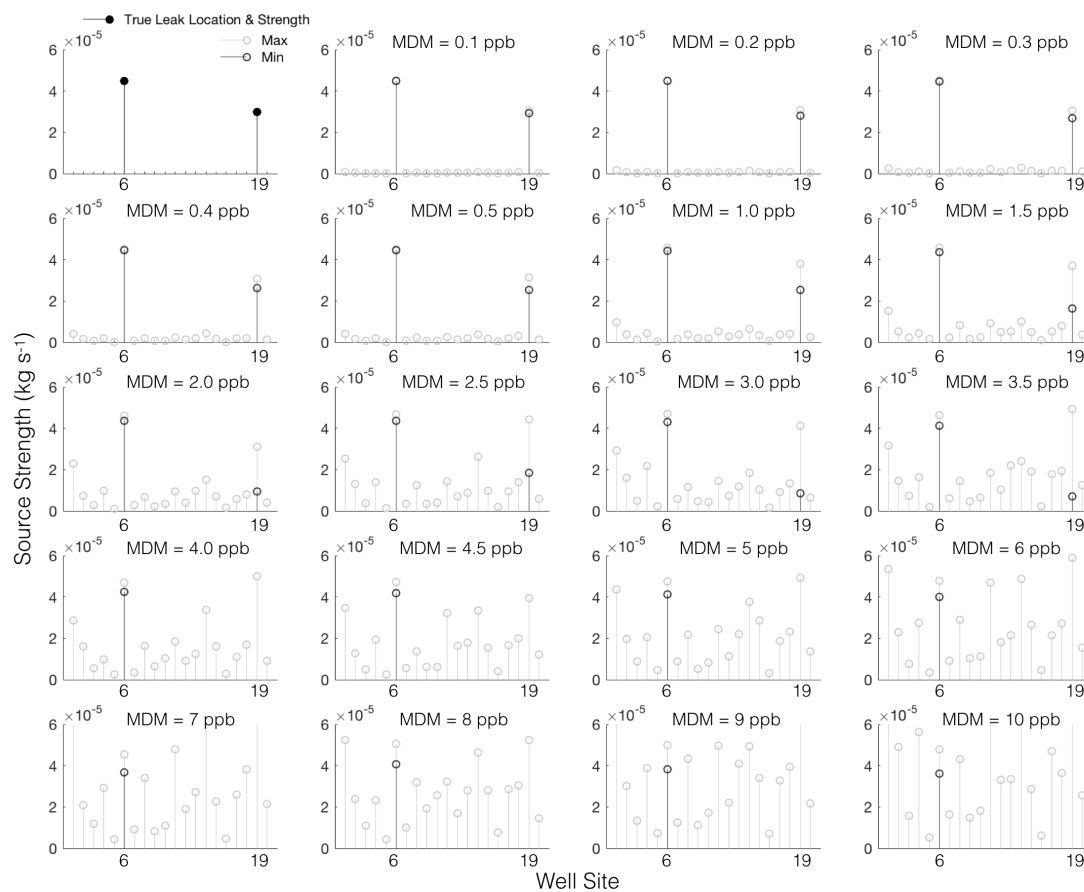
Figure 5: Top left panel shows well site numbers (x-axis) and corresponding "true" leak rates (y-axis), and remaining panels show resulting leak rate (y-axis) at each well site (x-axis) from non-bootstrap least squares fit to synthetic observations perturbed with model-data mismatch (MDM) noise shown, for the 8-beam case. Open circles show locations and strengths of all non-zero solutions.
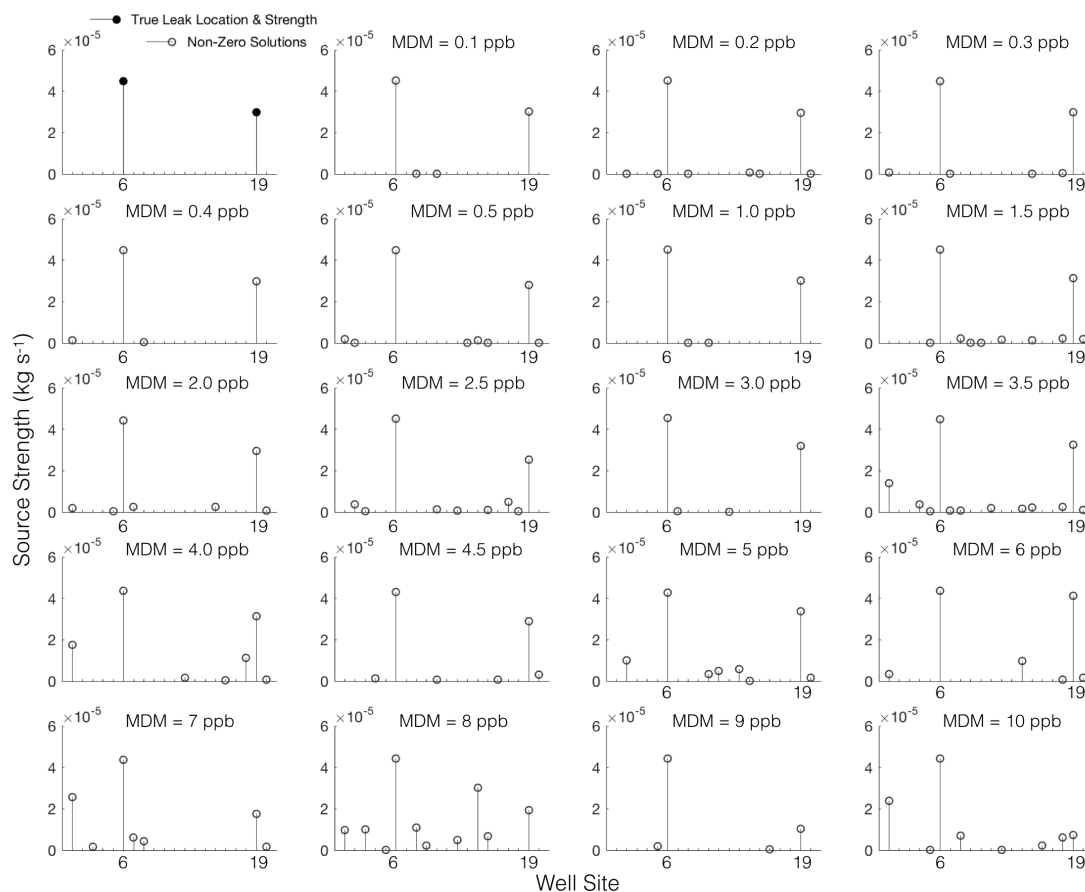
Figure 6: Top left panel shows well site numbers (x-axis) and corresponding "true" leak rates (y-axis), and remaining panels show NZMB results (y-axis) for each well site location (x-axis) with synthetic observations perturbed with model-data mismatch (MDM) noise shown, for the 8-beam case. Light gray (black) open circles show locations and strengths of the maximum (minimum) of 1000
5   **bootstrap operations. Minimum values of zero are not plotted.**
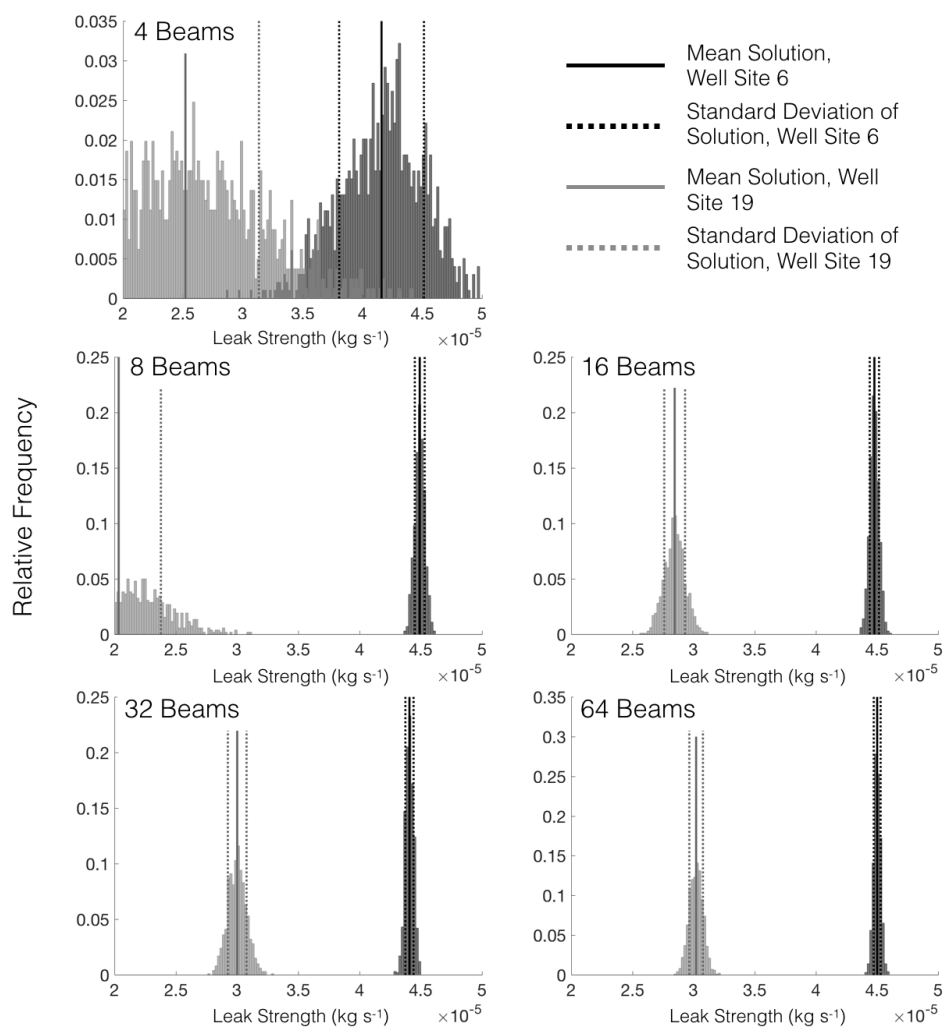
Figure 7: Histograms of source strength, with mean ± 1 standard deviation shown with vertical lines for well site 6 (black) and well site 19 (gray), for each beam configuration, and with 2 ppb model-data mismatch uncertainty. Note that x-axes are truncated at 2E-5 kg s^{-1} (lower bound) and 5E-5 kg s^{-1} (lower bound) for scale.
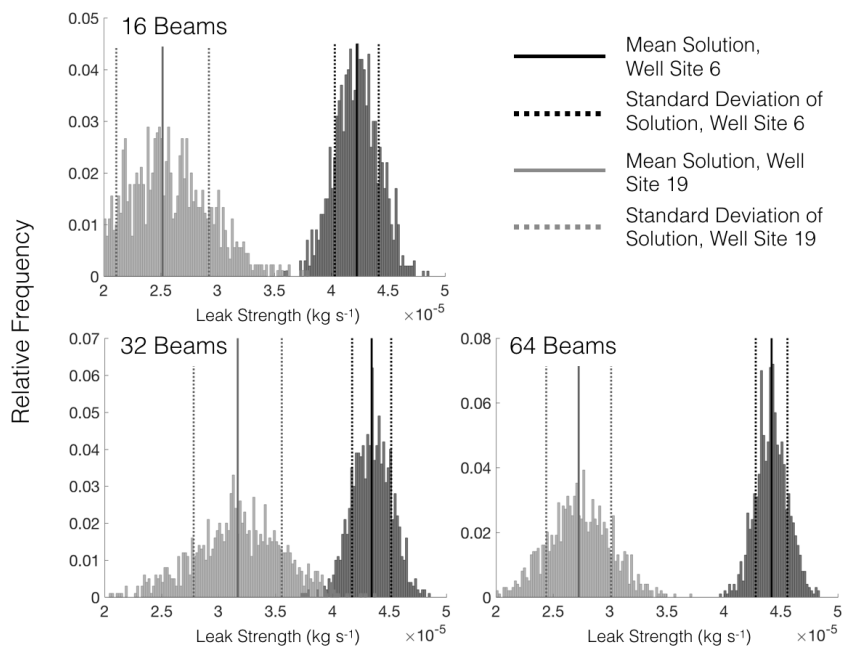
Figure 8: Histograms of source strength, with mean ± 1 standard deviation shown with vertical lines for well site 6 (black) and well site 19 (gray), for 16, 32 and 64 beam configurations, and with 10 ppb model-data mismatch uncertainty.
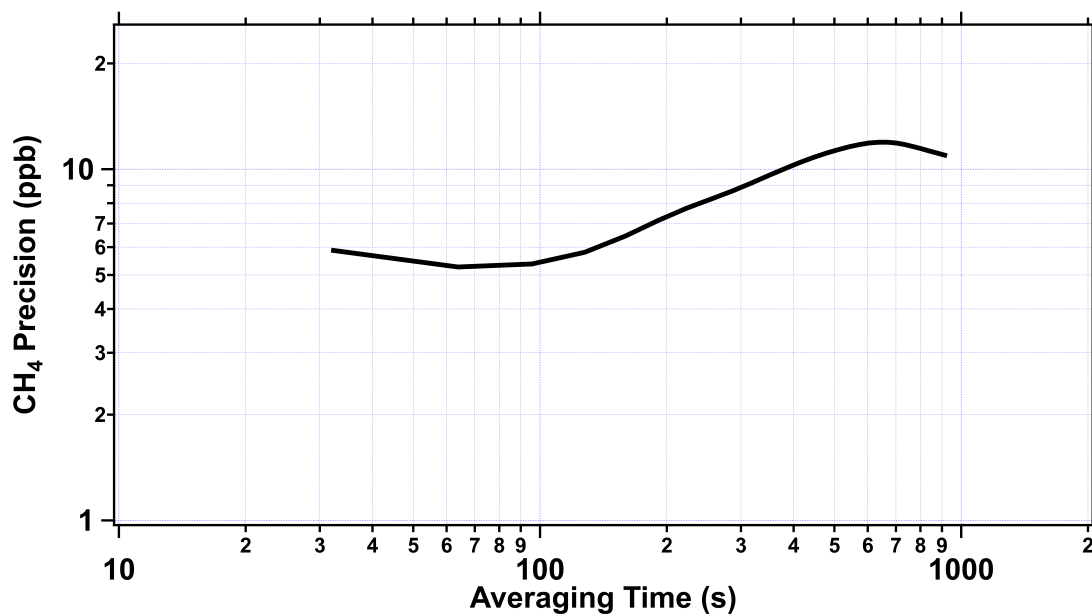
Figure 9: Allan deviation plot showing changes in measurement precision with averaging time from field data collected at Table Mountain on January 26th, 2017.
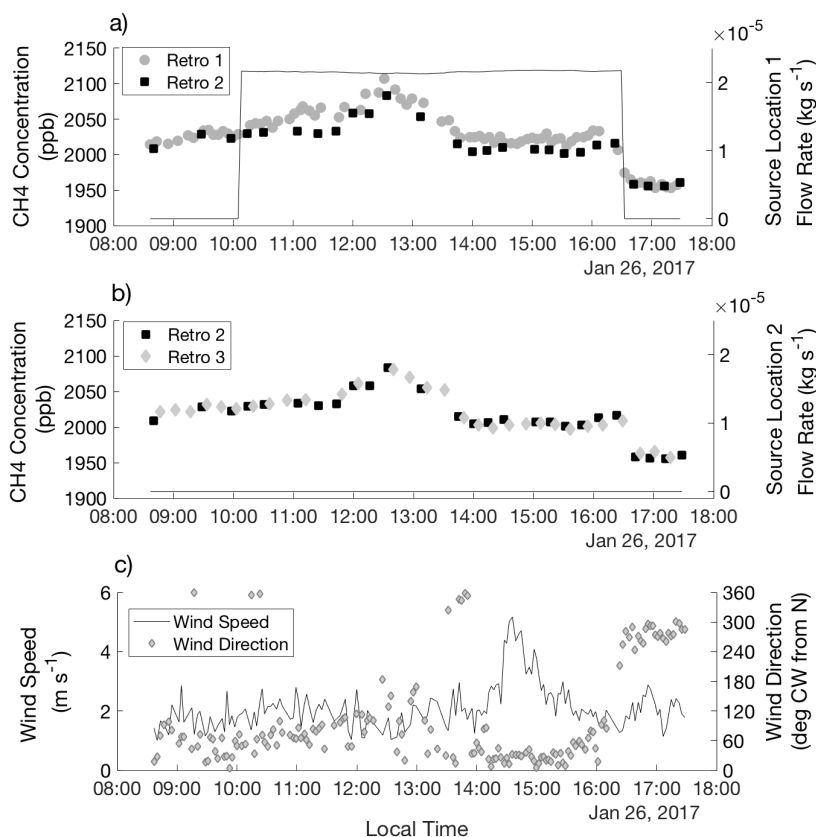
Figure 10: Line integrated atmospheric CH$_4$ concentrations measured on January 26, 2017 along beam paths to retros 1 and 2 (a), and to retros 2 and 3 (b), and wind speed and wind direction (c). Each point represents a 2-minute averaged concentration. Gray and black points and left-hand axes of panels (a) and (b) show CH$_4$ concentration. The black line and right-hand axis in panel (a) shows the flow rate at source location 1 (bounded by retros 1 and 2) and the black line and right-hand axis in panel b shows the flow rate at source location 2 (bounded by retros 2 and 3). In panel (c), the black line and left-hand axis show wind speed and the gray diamonds and right-hand axis show wind speed.
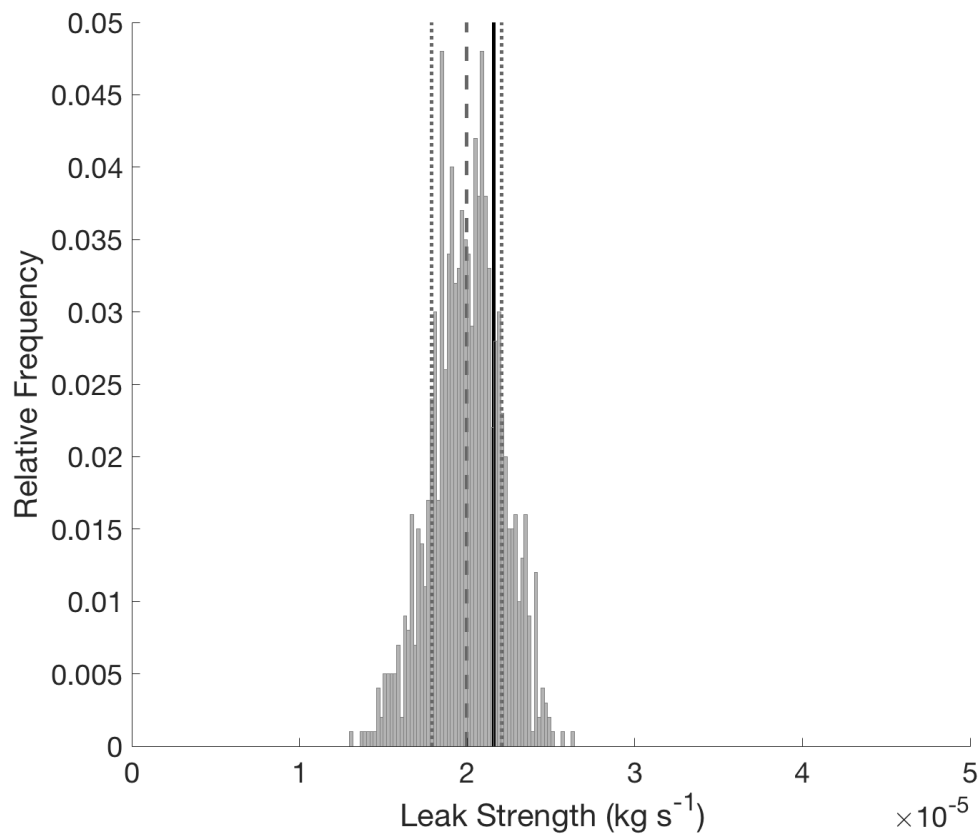
Figure 11: Histogram of NZMB estimated source strength at source location 1, with dashed line showing the bootstrap mean and thin dotted lines showing ± 1 standard deviation. The thick black line shows the true leak strength at source location 1 (2.1 E-5 kg s^{-1}).
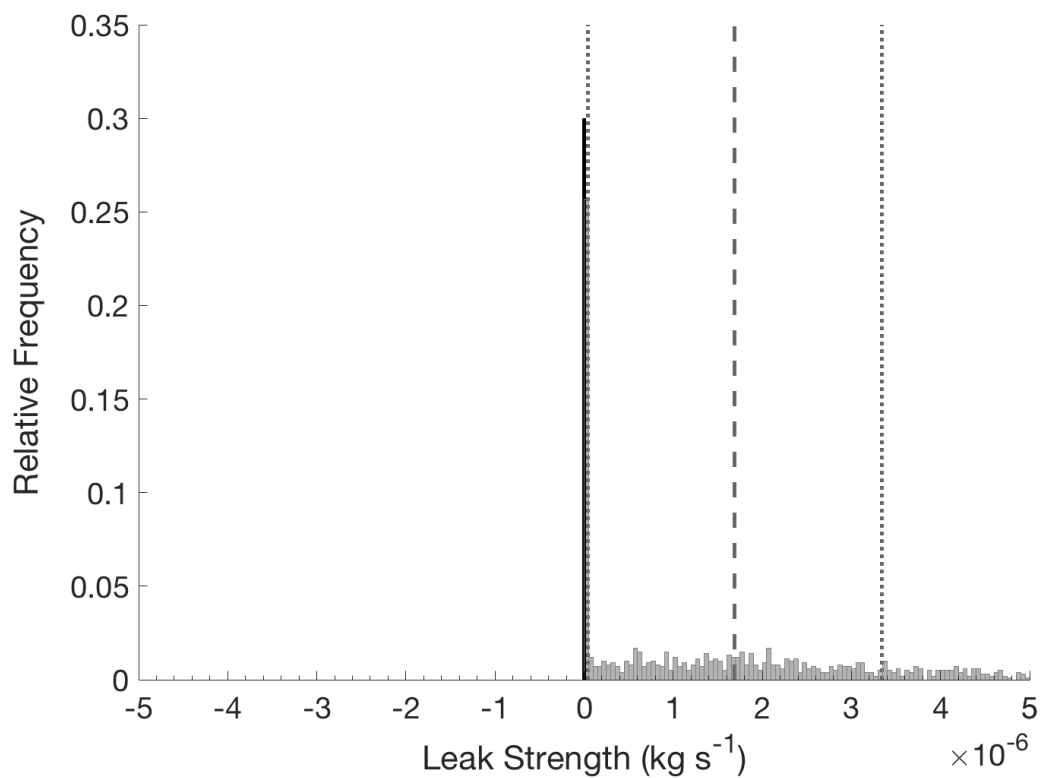
Figure 12: Histogram of NZMB estimated source strength at source location 2, with dashed line showing the bootstrap mean and thin dotted lines showing ± 1 standard deviation. The thick black line shows the true leak strength at source location 2 (0 kg s⁻¹). The presence of 0 kg s⁻¹ in the histogram triggers acceptance of the null hypothesis (that the emissions rate at this site is zero).

Number of Beams	Well Site 6 Mean Strength	Leak One 1 s. d.	Well Site 19 Mean Strength	Leak Two 1 s. d.
4	4.2E-5 kg s^{-1}	0.4E-5 kg s^{-1}	2.5E-5 kg s^{-1}	0.6E-5 kg s^{-1}
8	4.5E-5 kg s^{-1}	0.4E-6 kg s^{-1}	2.0E-5 kg s^{-1}	0.3E-5 kg s^{-1}
16	4.5E-5 kg s^{-1}	0.4E-6 kg s^{-1}	2.8E-5 kg s^{-1}	0.9E-6 kg s^{-1}
32	4.4E-5 kg s^{-1}	0.3E-6 kg s^{-1}	3.0E-5 kg s^{-1}	0.8E-6 kg s^{-1}
64	4.5E-5 kg s^{-1}	0.3E-6 kg s^{-1}	3.0E-5 kg s^{-1}	0.6E-6 kg s^{-1}
True Leak: 4.5E-5 kg s^{-1}			**True Leak: 3.0E-5** kg s^{-1}	

5   **Table 1:** NZMB Solutions for leak strength of true leaks, given 2 ppb model-data mismatch uncertainty, for each beam configuration.

	Source Location 1	Source Location 2
Controlled Leak Time On:	10:08	NA
Controlled Leak Time Off:	16:30	NA
Measured Mean Flow Rate:	2.1 E-5 ± 0.01E-5 kg s^{-1}	0.0 ± 0.0 kg s^{-1}
Non-Bootstrap Solution:	2.3 E-5 kg s^{-1}	0.2 E-5 kg s^{-1}
NZMB Solution:	2.0 E-5 ± 0.2 E-5 k/s	0.0 ± 0.0 kg s^{-1}

Table 2: Controlled methane release flow rates and 1 standard deviation for each field experiment, including local time that leak was turned on and off.